Electronic Research Archive

https://www.aimspress.com/journal/era

ERA, 33(10): 6375–6390.
DOI: 10.3934/era.2025281
Received: 26 August 2025
Revised: 20 October 2025
Accepted: 20 October 2025
Published: 27 October 2025

Research article

An unconditionally stable hybrid numerical method for the gradient flow for the high-order Modica–Mortola functional

Hyundong Kim[1,2], Zhengang Li[3], Xinpei Wu[4], Hyunho Shin[4], Yunjae Nam[3] and Junseok Kim[4,*]

[1] Department of Mathematics and Physics, Gangneung-Wonju National University, Gangneung 25457, Republic of Korea

[2] Institute for Smart Infrastructure, Gangneung-Wonju National University, Gangneung 25457, Republic of Korea

[3] Program in Actuarial Science and Financial Engineering, Korea University, Seoul 02841, Republic of Korea

[4] Department of Mathematics, Korea University, Seoul 02841, Republic of Korea

* **Correspondence:** Email: cfdkim@korea.ac.kr.

Abstract: This paper presents a numerically stable, time-accurate algorithm for simulating the gradient flow associated with the Modica–Mortola functional with a uniformly spaced multi-well potential. The scheme uses operator splitting; the nonlinear component is updated analytically, while the linear part is advanced by a Fourier spectral discretization. The method is unconditionally stable, preserves pointwise boundedness independently of the time step size, and attains spectral accuracy in space and first-order accuracy in time. We provide a theoretical analysis establishing unconditional stability and boundedness, and present comprehensive numerical experiments that demonstrate the accuracy and robustness of the proposed approach.

Keywords: Modica–Mortola model; high-order multi-well free energy; multi-phase system; Fourier spectral approach; stable scheme

1. Introduction

The Modica–Mortola (MM) functional is a classical model in the calculus of variations and geometric measure theory, originally proposed to characterize interfacial energy in materials, particularly in phase coexistence systems [1]. By introducing a parameter controlling interface thickness, it enables smooth approximations of sharp interfaces and provides a bridge between diffuse interface models and sharp interface models [2]. As the parameter tends to zero, the functional converges mathematically to the classical perimeter functional. Due to its computational

efficiency and accurate modeling of interfaces, the MM functional has been widely applied in image segmentation [3,4], phase transition modeling [5], and materials science [6]. The MM functional serves as a key tool for studying multiphase image segmentation dynamics in contrast with binary image segmentation [7]. The MM functional has been widely studied. Jung et al. [8] introduced a multiphase segmentation framework based on MM diffuse-interface energy, and they combined a sine potential for enforcing binary phases with a data term. As interface width ϵ goes to zero, the model recovers the Mumford–Shah functional and guarantees the existence and compactness of minimizers. An alternating-minimization algorithm with a convex-concave splitting resolves nonconvexity. Numerical experiments on synthetic, medical (MRI), noisy, and blurred images demonstrated superior boundary fidelity, noise robustness, and editability compared to prior methods. Within the phase-field method for solving optimal packing and Cheeger-type partitioning problems, the work of [9] focuses on α-Cheeger configurations and rigorously demonstrates that both maximum- and sum-based minimizers converge to optimal packings composed of equally sized balls. They proposed the MM phase-field variational convergence framework to compute α-Cheeger constants and clusters, enabling direct gradient-based optimization. Wang and Kim [4] proposed a modified MM equation that used a phase-dependent interfacial functional to maintain sharp interfaces. In the classical MM model, using a constant interfacial parameter caused transition layers to broaden as phase differences grew; by contrast, their adaptive function narrowed the interface where the phase-field gradient was larger. Computational tests confirmed superior interface resolution over the conventional MM model. Ham et al. [10] developed an unconditionally stable numerical algorithm with second-order temporal accuracy, using operator splitting method [11, 12] to solve the gradient flow equation associated with the MM energy featuring uniformly spaced multi-well potentials. They solved the nonlinear sine term analytically and the linear diffusion term via a Fourier spectral method, and then they proved that the numerical solution remained bounded and stable for any time step size. Through theoretical analysis and numerical tests, they confirmed second-order accuracy in time, spectral-order accuracy in space, and robustness in stability and convergence tests. Wilbuer et al. [2] developed a geometrically exact, 3D finite element phase-field model to study deformation-dependent interface elasticity in mechanically driven phase transformations. They coupled an Allen–Cahn-type diffuse-interface model which is based on the MM double-well energy potential, with homogenized bulk descriptions and a Ginzburg–Landau viscosity term. A monolithic Newton solver handled the resulting nonlinear system. Numerical examples demonstrated that higher interface energies accelerated inclusion coalescence and anisotropic responses at phase boundaries.

This paper proposes a stable numerical scheme, independent of time step size, designed for the gradient flow associated with the MM energy functional incorporating a higher-order potential:

$$\frac{\partial \phi(\mathbf{x}, t)}{\partial t} = -\frac{F'_\alpha(\phi(\mathbf{x}, t))}{\epsilon^2} + \Delta\phi(\mathbf{x}, t), \tag{1.1}$$

$$\mathbf{n} \cdot \nabla\phi = 0 \text{ on } \partial\Omega. \tag{1.2}$$

Here, $\phi(\mathbf{x}, t)$ denotes the phase-field variable defined over the spatial domain $\mathbf{x} \in \Omega$ and temporal variable t. The parameter ϵ governs the width of the transition interface, and $\mathbf{n}$ denotes the unit normal vector pointing outward on the boundary $\partial\Omega$. Equation (1.1) corresponds to the gradient descent evolution associated with the MM energy functional [8].

$$\mathcal{E}(\phi) := \int_{\Omega} \left[\frac{F_\alpha(\phi(\mathbf{x}, t))}{\epsilon^2} + \frac{1}{2}|\nabla \phi|^2 \right] d\mathbf{x}. \tag{1.3}$$

The following high-order multiple-well free energy potential is considered:

$$F_\alpha(\phi) = \frac{1}{\sqrt{\alpha}}(1 - \cos^\alpha(\pi\phi)), \tag{1.4}$$

where α is an even integer, see Figure 1 for $F_\alpha(\phi)$ and $F'_\alpha(\phi)$ with various α values. Figure 1(a) shows the behavior of the function $F_\alpha(\phi)$ as the parameter α varies. For the MM functional, the free energy potential is a periodic function. When $\alpha = 2$, $F_\alpha(\phi)$ exhibits the steepest gradients near integer values of ϕ. As α increases, the gradients of $F_\alpha(\phi)$ near integer ϕ gradually decrease, and the curve becomes flatter and less distinctive. Figure 1(c) presents the negative derivative of the function, $-F'_\alpha(\phi)$. When ϕ is an integer, the curves exhibit similar steepness regardless of the value of α. However, when ϕ is near non-integer values, such as -0.5 or 0.5, the curves become significantly flatter as α increases.

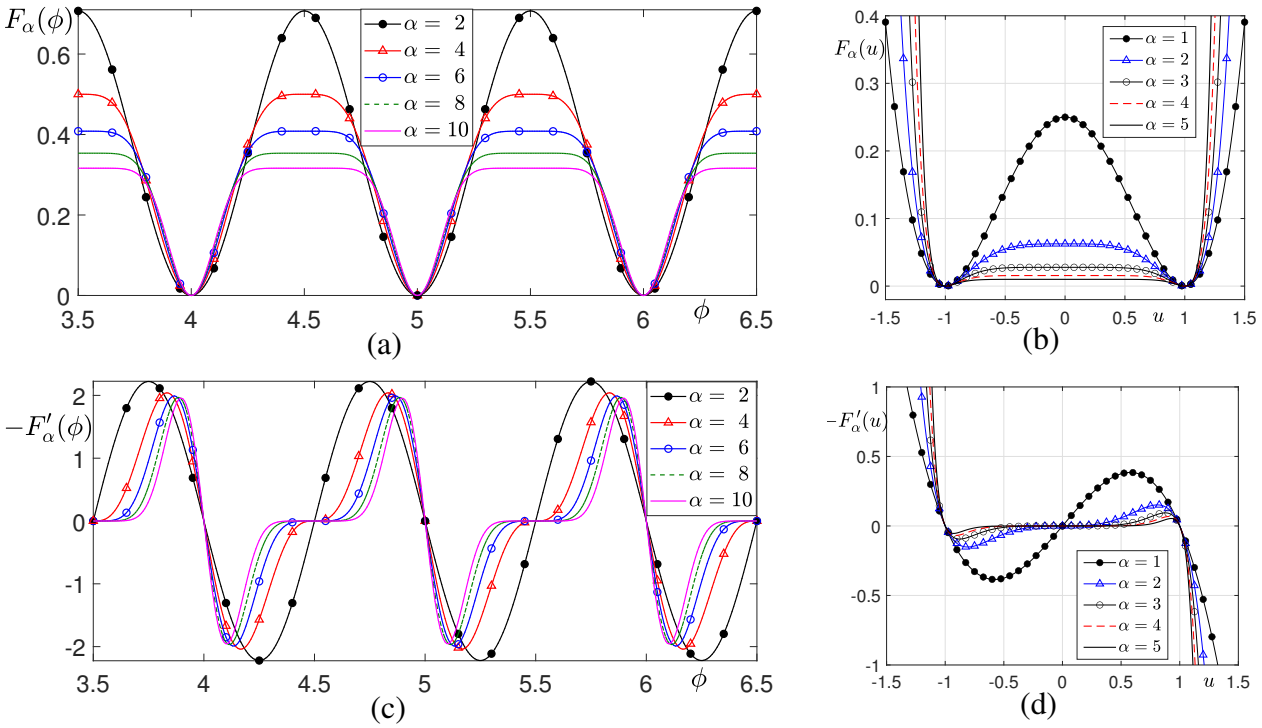

Figure 1. (a) $F_\alpha(\phi) = 1/\sqrt{\alpha}(1 - \cos^\alpha(\pi\phi))$ and (c) $-F'_\alpha(\phi) = -\sqrt{\alpha}\pi \sin(\pi\phi)\cos^{\alpha-1}(\pi\phi)$ on $[3.5,\ 6.5]$. (b) $F_\alpha(\phi) = (\phi^{2\alpha}-1)^2/(4\alpha^2)$ and (d) $-F'_\alpha(\phi) = -\phi^{2\alpha-1}(\phi^{2\alpha}-1)/\alpha$ on $[-1.5,\ 1.5]$. Figures (b) and (d) are reprinted from [13] under the terms of the CC BY License.

Remark. We adopt a high-order multi-well free energy with an even integer parameter α in order to control phase purity and interface sharpness in a direct manner. As α increases the restoring force near each well becomes stronger while the barrier region between consecutive wells becomes flatter. This combination suppresses intermediate values, delays barrier crossings, and yields crisper multi-phase partitions. Such behavior is desirable in applications that require near-pure phases and thin interfaces,

for example multi-phase segmentation, grain or domain partitioning, and multi-component separation under weak mixing.

We couple the interface parameter through the normalization

$$\epsilon(\alpha) = \epsilon_0/\sqrt{\alpha},$$

which keeps interface thickness and front speed approximately invariant across α. This allows fair comparisons and avoids artificial sharpening due to scaling. The local structure explains the modelling effect. With

$$F'_\alpha(\phi) = \sqrt{\alpha}\,\pi\,\sin(\pi\phi)\,\cos^{\alpha-1}(\pi\phi),$$

the curvature at a well location $m \in \mathbb{Z}$ satisfies

$$F''_\alpha(m) = \sqrt{\alpha}\,\pi^2.$$

Therefore each well remains quadratic with a stiffness that grows like $\sqrt{\alpha}$. At the barrier $\phi = m + \frac{1}{2}$ the derivative vanishes to high order because the cosine factor vanishes with multiplicity that increases with α, which flattens the barrier region and enhances metastability.

We provide practical guidance for the choice of α. Moderate values such as $\alpha = 4$ or $\alpha = 6$ already strengthen phase purity without excessive stiffness. Larger values such as $\alpha \geq 8$ are suited to enforce very thin interfaces and hard phases under noisy data or strong multi-phase competition. The nonlinear stage uses an analytic pointwise update; therefore, the added stiffness near the wells does not force a smaller time step.

For a comparison with the binary AC equation with a high-order double-well free energy potential [13], see Figure 1(b),(d) for the free energy potential $F_\alpha(\phi) = (\phi^{2\alpha} - 1)^2/(4\alpha^2)$ and its derivative $-F'_\alpha(\phi) = -\phi^{2\alpha-1}(\phi^{2\alpha} - 1)/\alpha$. Figure 2 demonstrates that wave propagation under high initial noise strongly depends on the parameter α. For $\alpha = 1$, large oscillations persist across all times, indicating poor noise suppression. In contrast, $\alpha = 2$ and $\alpha = 5$ effectively dampen noise, with $\alpha = 5$ showing the smoothest and most stable wave profiles. At later times, larger α values yield clear separation into stable states, while smaller $\alpha = 1$ values remain unstable. This behavior arises from the use of a high-order double-well potential and highlights a valuable feature for data classification, namely its robustness against noisy data. Consequently, the proposed high-order multiple-well free energy potential can be regarded as a counterpart to the high-order double-well free energy potential.

This study considers the gradient flow associated with the MM functional incorporating higher-order, equally spaced multi-well potentials capable of capturing multiphase dynamics. An accurate and computationally efficient numerical approximation is achieved via a Lie-type operator splitting approach. The proposed scheme is unconditionally stable by establishing that the numerical solution remains uniformly bounded under the initial condition. Furthermore, we investigate how altering the degree of the polynomial potential influences the behavior of front propagation during phase transitions. Emphasis is placed on the role of higher-order terms in determining the propagation velocity, interfacial sharpness, and morphological evolution, and this thereby provides new insights into the capacity of the MM model to describe intricate physical phenomena.

The primary purpose of this article is to propose a simple and robust model for the high-order potential MM gradient flow. The scheme applies a Lie operator splitting method, where the

nonlinear and linear stages are treated separately. The study emphasizes the importance of the modeling choice and its impact on stability and numerical behavior. For completeness, we also describe how a symmetric Strang composition can achieve second-order temporal accuracy within the same framework.

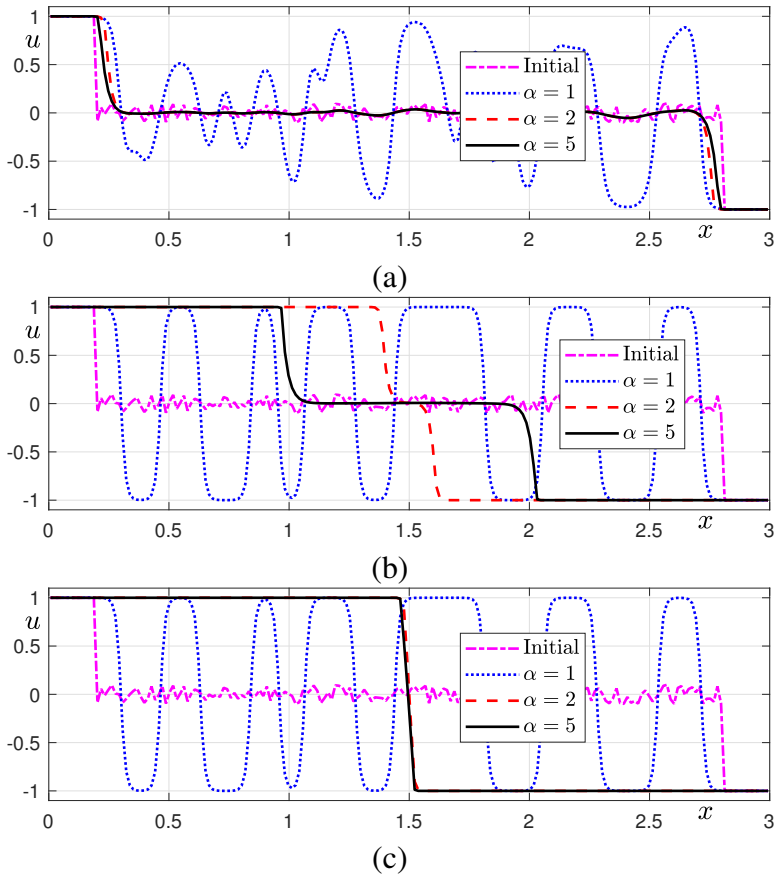

Figure 2. (a)–(c) show wave propagations under an initially higher noise level at $t = 0.0001,\ 0.002$, and 0.035, respectively, for $\alpha = 1,\ 2$, and 5. Figures are reprinted from [13] under the terms of the Creative Commons Attribution (CC BY) License.

The article is structured in the following manner. Section 2 outlines the proposed numerical method. Section 3 reports the computational results. Section 4 provides a summary of the study's main results.

2. Numerical solution algorithm

This section introduces an unconditionally stable time integration scheme for solving the governing equation derived from the MM functional with a high-order, equally spaced 2D multi-well potential. We consider the numerical approximation of Eq (1.1) over the domain $\Omega = (L_x, R_x) \times (L_y, R_y)$. Let N_x and N_y be positive integers and let $h = (R_x - L_x)/N_x$ be the uniform mesh size. The spatial domain is discretized as $\Omega_h = \{(x_i, y_j) \mid x_i = L_x + (i - 0.5)h,\ y_j = L_y + (j - 0.5)h,\ 1 \le i \le N_x,\ 1 \le j \le N_y\}$. We denote the discrete phase-field variable at n-th time level by $\phi_{ij}^n = \phi(x_i, y_j, n\Delta t)$, with Δt representing the time step size.

To obtain a numerical solution of Eq (1.1), we use an operator splitting approach [14, 15] and reformulate the equation as follows:

$$\frac{\partial \phi(\mathbf{x}, t)}{\partial t} = \mathcal{N}(\phi(\mathbf{x}, t)) + \mathcal{L}(\phi(\mathbf{x}, t)), \tag{2.1}$$

where $\mathcal{N}(\phi(\mathbf{x}, t)) = -F'_{\alpha}(\phi((\mathbf{x}), \mathbf{t}))/\epsilon^2$ and $\mathcal{L}(\phi(\mathbf{x}, t)) = \Delta\phi(\mathbf{x}, t)$. Following the Lie-type operator splitting [16], we first integrate the nonlinear subproblem (2.2) with the initial condition

$$\psi_1(\mathbf{x}, 0) = \phi(\mathbf{x}, n\Delta t),$$

to obtain the intermediate state $\psi_1(\mathbf{x}, \Delta t)$. Then, we solve the linear subproblem (2.3) with

$$\psi_2(\mathbf{x}, 0) = \psi_1(\mathbf{x}, \Delta t)$$

to obtain $\psi_2(\mathbf{x}, \Delta t)$, and we set $\phi(\mathbf{x}, (n + 1)\Delta t) = \psi_2(\mathbf{x}, \Delta t)$, and

$$\frac{\partial \psi_1(\mathbf{x}, t)}{\partial t} = \mathcal{N}(\psi_1(\mathbf{x}, t)). \tag{2.2}$$

$$\frac{\partial \psi_2(\mathbf{x}, t)}{\partial t} = \mathcal{L}(\psi_2(\mathbf{x}, t)). \tag{2.3}$$

From Eq (2.2) and $F'_{\alpha}(\phi) = \sqrt{\alpha}\pi \sin(\pi\phi)\cos^{\alpha-1}(\pi\phi)$, we have

$$\frac{\partial \psi_1(\mathbf{x}, t)}{\partial t} = -\frac{\sqrt{\alpha}\pi}{\epsilon^2} \sin(\pi\psi_1(\mathbf{x}, t)) \cos^{\alpha-1}(\pi\psi_1(\mathbf{x}, t)). \tag{2.4}$$

Using $\sin(\pi u)\cos^{\alpha-1}(\pi u) = \frac{1}{2}\sin(2\pi u)\cos^{\alpha-2}(\pi u)$, Eq (2.4) becomes

$$\frac{d\psi_1(\mathbf{x}, t)}{dt} = A^n(\mathbf{x})\ \sin(2\pi\psi_1(\mathbf{x}, t)), \tag{2.5}$$

with the frozen-coefficient choice

$$A^n(\mathbf{x}) = -\frac{\sqrt{\alpha}\,\pi}{2\varepsilon^2}\cos^{\alpha-2}(\pi\psi_1(\mathbf{x}, 0)) = -\frac{\sqrt{\alpha}\,\pi}{2\varepsilon^2}\cos^{\alpha-2}(\pi\phi(\mathbf{x}, n\Delta t)), \tag{2.6}$$

which is independent of time t on $[t_n, t_{n+1}]$, $t_n := n\Delta t$, and is frozen at the n-th time level.

If $\sin(2\pi\psi_1) \equiv 0$ on $[t_n, t_{n+1}]$, then $\psi_1(\mathbf{x}, t) \equiv \psi_1(\mathbf{x}, 0)$. Otherwise,

$$\frac{d\psi_1}{\sin(2\pi\psi_1)} = A^n(\mathbf{x})dt. \tag{2.7}$$

Set $v = 2\pi\psi_1$ so that $dv = 2\pi d\psi_1$. Then,

$$\frac{1}{2\pi}\int \frac{dv}{\sin v} = \int A^n(\mathbf{x})dt. \tag{2.8}$$

Equivalently, writing the left-hand side as

$$\frac{1}{2\pi}\int \frac{\sin v}{1-\cos^2 v}dv = -\frac{1}{2\pi}\int \frac{d(\cos v)}{1-(\cos v)^2} = \frac{1}{4\pi}\ln\frac{1-\cos v}{1+\cos v}, \tag{2.9}$$

we obtain

$$\frac{1}{4\pi}\ln\frac{1-\cos(2\pi\psi_1(\mathbf{x},t))}{1+\cos(2\pi\psi_1(\mathbf{x},t))} = A^n(\mathbf{x})\,t + C(\mathbf{x}), \tag{2.10}$$

with

$$C(\mathbf{x}) = \frac{1}{4\pi}\ln\frac{1-\cos(2\pi\psi_1(\mathbf{x},0))}{1+\cos(2\pi\psi_1(\mathbf{x},0))}. \tag{2.11}$$

The solution to Eq (2.10) is given by

$$\begin{aligned}\psi_1(\mathbf{x},t) = \lfloor\phi(\mathbf{x},n\Delta t)\rfloor + \frac{1+\operatorname{sgn}(\bar{\phi}(\mathbf{x},n\Delta t)-0.5)}{2}\\ +\frac{\operatorname{sgn}(0.5-\bar{\phi}(\mathbf{x},n\Delta t))}{2\pi}\arccos\left(\frac{1-e^{4\pi At+4\pi C(\mathbf{x})}}{1+e^{4\pi At+4\pi C(\mathbf{x})}}\right),\end{aligned} \tag{2.12}$$

where $C(\mathbf{x}) = \dfrac{1}{4\pi}\ln\dfrac{1-\cos(2\pi\phi(\mathbf{x},n\Delta t))}{1+\cos(2\pi\phi(\mathbf{x},n\Delta t))}$ and $\bar{\phi}(\mathbf{x},n\Delta t) = \phi(\mathbf{x},n\Delta t) - \lfloor\phi(\mathbf{x},n\Delta t)\rfloor$. Here, $\operatorname{sgn}(x)$ denotes the usual sign function and $\lfloor x\rfloor$ represents the integer part of x, defined by $\lfloor x\rfloor = \sup\{m\in\mathbb{Z} : m\le x\}$.

Next, we solve Eq (2.3):

$$\frac{\partial\psi_2(\mathbf{x},t)}{\partial t} = \Delta\psi_2(\mathbf{x},t). \tag{2.13}$$

By applying the Fourier spectral approach with the initial state $\psi_2(\mathbf{x},0) = \psi_1(\mathbf{x},\Delta t)$, one can implement the method for Eq (2.13). After solving Eq (2.13), we obtain $\phi(\mathbf{x},(n+1)\Delta t) = \psi_2(\mathbf{x},\Delta t)$. A detailed description of the Fourier spectral method can be found in [10].

The presented numerical method for the high-order MM functional Eq (1.1) exhibits unconditional stability. Through the Lie-type operator splitting Eq (2.1), the nonlinear stage Eq (2.2) is solved analytically by the frozen-coefficient method, and the linear stage Eq (2.3) is advanced using the Fourier spectral approach. Each step of this splitting strategy is independently unconditionally stable, which ensures that the overall numerical solution remains uniformly bounded for any time-step size. Consequently, the method achieves both robustness and accuracy without the restrictions typically imposed by explicit schemes [17].

Remark. This work studies a MM gradient flow with a high-order multi-well potential and uses a Lie operator splitting as a simple and robust modelling vehicle. The parameter α tunes phase purity and interface sharpness. We use the normalization $\epsilon(\alpha) = \epsilon_0/\sqrt{\alpha}$ so that interface thickness and front speed remain comparable across α. The baseline integrator keeps stepwise complexity low through one pointwise nonlinear update and one cosine-spectral diffusion update.

The approach is distinct from [10]. That study targets the standard MM model and develops a second-order Strang splitting with unconditional stability and pointwise boundedness, supported by manufactured solution evidence of temporal order near two together with full analytical proofs. Our emphasis is the modelling effect of the high-order potential and its numerical behavior under parameter sweeps. We report convergence tests in time and space and design experiments that expose features specific to the high-order potential, including alpha sweeps for phase purity, interface control under a fixed normalization, robustness to noise, and delayed barrier crossings.

When higher temporal accuracy is required, a symmetric Strang composition that applies a half step of the nonlinear stage (2.2) on $[t_n,\ t_n + \frac{\Delta t}{2}]$, a full step of the linear stage (2.3) on $[t_n,\ t_n + \Delta t]$, and a half step of the nonlinear stage (2.2) on $[t_n + \frac{\Delta t}{2},\ t_{n+1}]$ attains second-order accuracy in time while retaining the same building blocks. Let $S_{\mathcal{N}}(t)$ and $S_{\mathcal{L}}(t)$ denote the exact subflows of the nonlinear and linear stages. The update is

$$\begin{aligned}\phi^{n+\frac{1}{2}} &= S_{\mathcal{N}}\Big(\tfrac{\Delta t}{2}\Big)\ \phi^n,\\ \phi^{n+\frac{1}{2}*} &= S_{\mathcal{L}}(\Delta t)\ \phi^{n+\frac{1}{2}},\\ \phi^{n+1} &= S_{\mathcal{N}}\Big(\tfrac{\Delta t}{2}\Big)\ \phi^{n+\frac{1}{2}*}.\end{aligned}$$

For smooth solutions, this symmetric composition attains second-order accuracy in time. The nonlinear substep uses the same analytic pointwise update as in the baseline scheme. The linear substep advances in cosine-spectral space under Neumann boundary conditions.

A complete, problem-specific proof of second-order convergence and stepwise energy stability for the present high-order multi-well model requires additional technical development. Second-order operator splitting with stability and convergence has been established for related nonlinear PDEs, including the good Boussinesq equation and reaction-diffusion equations in an energetic variational formulation [18]. These results offer transferable techniques and support the feasibility of the Strang design within our framework. A strictly dissipative modified energy can be adopted if stepwise energy stability is required, as discussed in recent analyses for Allen–Cahn type flows [19].

2.1. Energy stability: modified energy perspective

Let $\mathcal{E}(\phi)$ denote the classical MM energy used in this work. For our Lie operator splitting, a direct proof of stepwise dissipation $\mathcal{E}(\phi^{n+1}) \le \mathcal{E}(\phi^n)$ for the fully discrete scheme appears to be open. Instead, in line with the modern splitting theory for Allen–Cahn type flows, one can introduce a modified energy $\widetilde{\mathcal{E}}_\tau$ depending on the time step τ, for which the iterates satisfy

$$\widetilde{\mathcal{E}}_\tau(\phi^{n+1}) \ \le\ \widetilde{\mathcal{E}}_\tau(\phi^n), \qquad \widetilde{\mathcal{E}}_\tau(\phi) \ =\ \mathcal{E}(\phi) \ +\ O(\tau). \tag{2.14}$$

For the scalar Allen–Cahn equation, Li et al. [19] constructed such a $\widetilde{\mathcal{E}}_\tau$ and proved unconditional stability and strict dissipation, with $\widetilde{\mathcal{E}}_\tau$ coinciding with the classical energy up to $O(\tau)$; see also their explicit definition of $\widetilde{\mathcal{E}}_\tau$ and the inequality $\widetilde{\mathcal{E}}_\tau^{n+1} \le \widetilde{\mathcal{E}}_\tau^{n}$. Our MM gradient flow shares the same L^2 gradient flow structure, and we adopt this viewpoint. A fully rigorous construction of $\widetilde{\mathcal{E}}_\tau$ tailored to our multi-well potential is left as focused future work.

Remark. For OSM applied to gradient flow problems, a direct stepwise dissipation proof for the classical energy is subtle and remains open for the present MM model. In practice and in recent analysis, energy stability is justified through a modified energy $\widetilde{\mathcal{E}}_\tau$ for which the fully discrete scheme is strictly dissipative and which approximates the classical energy to $O(\tau)$. See [19] for a complete construction and proof in the Allen–Cahn case.

3. Computational experiments

We next conduct computational simulations of the gradient flow associated with the MM functional, which are carried out using an operator splitting strategy.

3.1. Convergence tests

We perform numerical tests to verify that the proposed method attains spectral accuracy in space and first-order accuracy in time. The initial condition is

$$\phi(x, y, 0) = \frac{1}{4}\left[4 - \tanh\left(\frac{x+0.2}{0.05}\right) - \tanh\left(\frac{x+0.5}{0.05}\right) - \tanh\left(\frac{x-0.2}{0.05}\right) - \tanh\left(\frac{x-0.5}{0.05}\right)\right], \tag{3.1}$$

on $\Omega = (-1, 1)^2$. We set $N_x = 128$, $N_y = 128$, $h = 1/64$, $\Delta t = 1.0\text{e-}5$, $\alpha = 10$, $\epsilon_0 = 0.2$, and $\epsilon = \epsilon_0/\sqrt{\alpha}$. For the spatial discretization, we fix $\Delta t = 1.0\text{e-}5$ and $T = 1.0\text{e-}4$. We gradually halve the spatial step size h, using $N = N_x = N_y = 64,\ 128,\ \ldots,\ 512$ with $h = 2/N$. The discrete l_2-norm error is defined as

$$\|e_{(N,2N)}\|_2 = \sqrt{\sum_{i=1}^{N_x}\sum_{j=1}^{N_y}\frac{1}{N_x N_y}\left(\Phi_{ij}^{N_t} - \frac{1}{4}\left(\phi_{2i-1,2j-1}^{N_t} + \phi_{2i-1,2j}^{N_t} + \phi_{2i,2j-1}^{N_t} + \phi_{2i,2j}^{N_t}\right)\right)^2}. \tag{3.2}$$

Here, $\Phi_{ij}^{N_t}$ denotes the numerical solution on the coarse grid with mesh size h, while $\phi_{2i-1,2j-1}^{N_t}$, $\phi_{2i-1,2j}^{N_t}$, $\phi_{2i,2j-1}^{N_t}$, and $\phi_{2i,2j}^{N_t}$ denote the numerical solutions at the corresponding four fine-grid points with mesh size $h/2$. Figure 3 illustrates the discrete l_2-norm error with respect to the number of grid points.

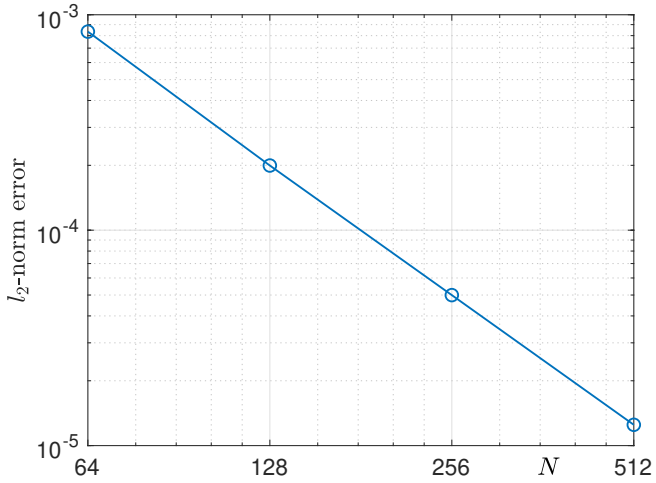

Figure 3. Discrete l_2-norm error versus the number of grid points on a log-log scale.

For the temporal study, we fix the final time $T = N_t\Delta t = 1.0\text{e-}4$ with $N_t \in \mathbb{N}$, and successively halve Δt. The discrete ℓ_2-error between consecutive refinements is

$$\left\|e^{(\Delta t, \Delta t/2)}\right\|_2 = \sqrt{\sum_{i=1}^{N_x}\sum_{j=1}^{N_y}\frac{1}{N_x N_y}\left(\phi_{ij}^{N_t} - \phi_{ij}^{2N_t}\right)^2},$$

where $\phi_{ij}^{N_t}$ is computed with time step Δt (after N_t steps) and $\phi_{ij}^{2N_t}$ with time step $\Delta t/2$ (after $2N_t$ steps), so that both approximations are evaluated at the same physical time T. The observed temporal order is

$$\log_2\left(\frac{\left\|e^{(\Delta t, \Delta t/2)}\right\|_2}{\left\|e^{(\Delta t/2, \Delta t/4)}\right\|_2}\right).$$

Table 1 reports the discrete ℓ_2 errors and the corresponding temporal convergence rates, and these results confirm first-order accuracy in time.

Table 1. Errors and rates of convergence in time.

$(\Delta t, \Delta t/2)$	Error	Rate
(1.00e-5, 5.00e-6)	2.3255e-4	
(5.00e-6, 2.50e-6)	1.1787e-4	0.98
(2.50e-6, 1.25e-6)	5.9338e-5	0.99
(1.25e-6, 6.25e-7)	2.9771e-5	1.00

3.2. Stability test

We study the stability behavior of the proposed numerical approach for the MM functional over the 2D domain $\Omega = (-1, 1)^2$, using the interface parameter $\epsilon = \epsilon_0/\sqrt{\alpha}$. In this experiment, we select $N_x = N_y = 128$, $h = 2/N_x$, $\epsilon_0 = 10h$, $\Delta t = 0.1h^2$, and $\alpha = 6$. We consider the initial condition as follows:

$$\phi(x, y, 0) = e^{x+0.3y} + \text{rand}(x, y), \tag{3.3}$$

where rand(x, y) is a random number between -0.3 and 0.3. For $\alpha = 6$, the temporal evolution of the initial condition in Eq (3.3) is illustrated in Figure 4. In more detail, Figure 4(a)–(f) show the temporal evolutions at $t = 0$, $10\Delta t$, $20\Delta t$, $50\Delta t$, $100\Delta t$, and $1000\Delta t$, respectively.

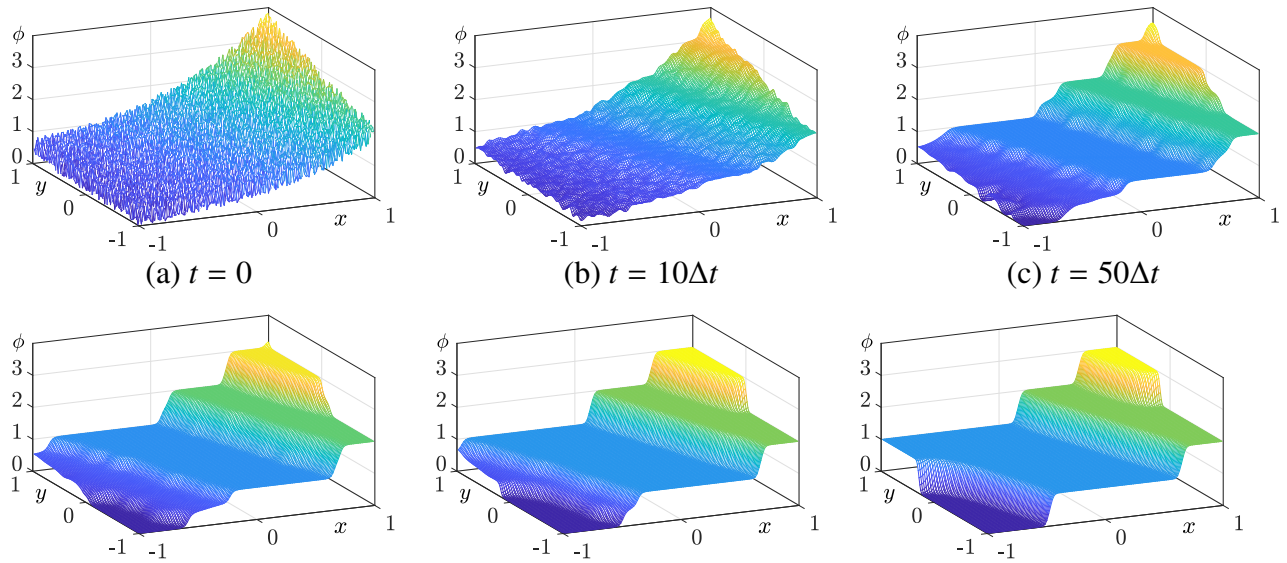

Figure 4. (a) Initial condition Eq (3.3). (b)–(f) are the temporal evolutions at $t = 10\Delta t$, $50\Delta t$, $100\Delta t$, $200\Delta t$, and $1000\Delta t$, respectively.

3.3. *Motion by mean curvature*

In this subsection, we examine the evolution driven by the mean curvature flow arising from the gradient descent of the MM functional within the 2D domain $\Omega = (-1, 1)^2$. The interfacial width is defined as $\epsilon = \epsilon_0/\sqrt{\alpha}$, where we choose $\epsilon_0 = 0.015$ for this particular setup. The computational grid consists of $N_x = N_y = 128$ nodes, leading to a spatial resolution of $h = 2/N_x = 2/N_y$. The time increment is fixed at $\Delta t = 0.001$, and the parameter α is assigned the value 6 in this numerical test.

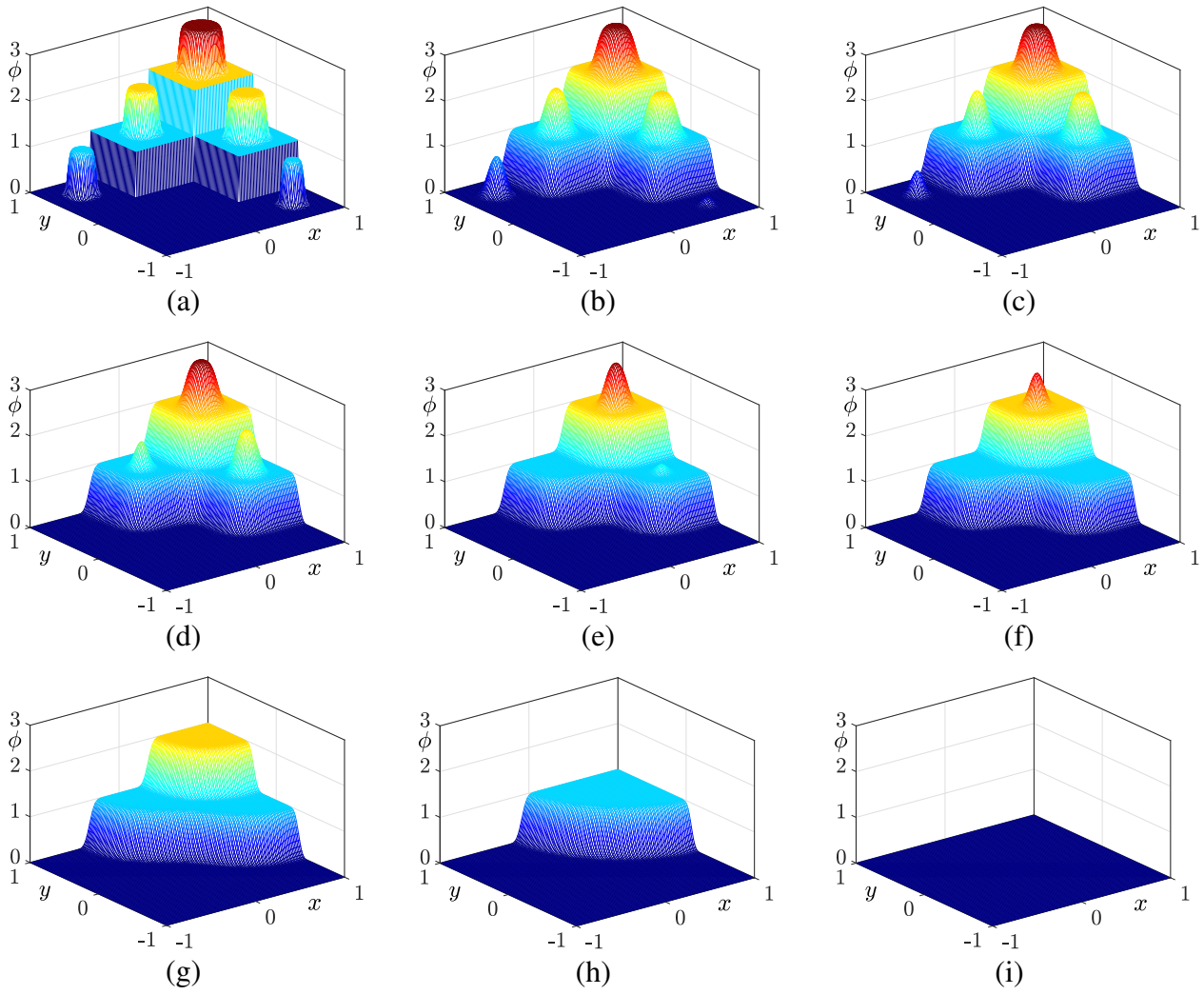

Figure 5. Snapshots at (a) initial condition, (b)–(i) are the temporal evolutions from the initial condition at times $t = 0.005$, $t = 0.007$, $t = 0.01$, $t = 0.015$, $t = 0.018$, $t = 0.05$, $t = 0.33$, and $t = 1$, respectively, for $\alpha = 6$.

As depicted in Figure 5, the simulation begins with a stair-like arrangement of cylinders positioned at heights 0, 1, and 2. The radii are assigned as 0.1, 0.125, 0.15, 0.175, and 0.2 in ascending order. The interface subsequently evolves under mean curvature flow. This serves as the initial condition for the computation.

$$\phi(x,y,0) = \begin{cases} 0.5\tanh(\frac{0.1-\sqrt{(x-0.67)^2+(y+0.67)^2}}{0.02}) + 0.5, & \frac{2}{3} \le x \le 1,\ y < \frac{1}{3}, \\ 0.5\tanh(\frac{0.125-\sqrt{(x+0.67)^2+(y-0.67)^2}}{0.02}) + 0.5, & x < \frac{1}{3},\ \frac{2}{3} \le y \le 1, \\ 0.5\tanh(\frac{0.15-\sqrt{x^2+(y-0.67)^2}}{0.02}) + 1.5, & \frac{1}{3} \le x < \frac{2}{3},\ \frac{2}{3} \le y \le 1, \\ 0.5\tanh(\frac{0.175-\sqrt{(x-0.67)^2+y^2}}{0.02}) + 1.5, & \frac{2}{3} \le x \le 1,\ \frac{1}{3} \le y < \frac{2}{3}, \\ 0.5\tanh(\frac{0.2-\sqrt{(x-0.67)^2+(y+1.33)^2}}{0.02}) + 2.5, & \frac{2}{3} \le x \le 1,\ \frac{2}{3} \le y \le 1, \\ 0, & \text{otherwise.} \end{cases} \tag{3.4}$$

3.4. Traveling wave solution

Let us consider the following condition on $\Omega = (0, 9) \times (0, 1)$:

$$\phi(x,y,0) = \begin{cases} 3, & \text{if } x < 0.5, \\ 2.5, & \text{if } 0.5 \le x < 2.5, \\ 2, & \text{if } 2.5 \le x < 3.5, \\ 1.5, & \text{if } 3.5 \le x < 5.5, \\ 1, & \text{if } 5.5 \le x < 6.5, \\ 0.5, & \text{if } 6.5 \le x < 8.5, \\ 0, & \text{otherwise.} \end{cases} \tag{3.5}$$

Here, we use $N_x = 180$, $N_y = 20$, $h = 0.05$, $\Delta t = 0.001$, and $\epsilon = 10h/\sqrt{\alpha}$ with $\alpha = 6$. Figure 6 illustrates the initial condition, as well as the traveling wave solutions at times $t = 10\Delta t$, $50\Delta t$, and $120\Delta t$. The solution evolves into a step-like profile with distinct plateaus as time progresses.

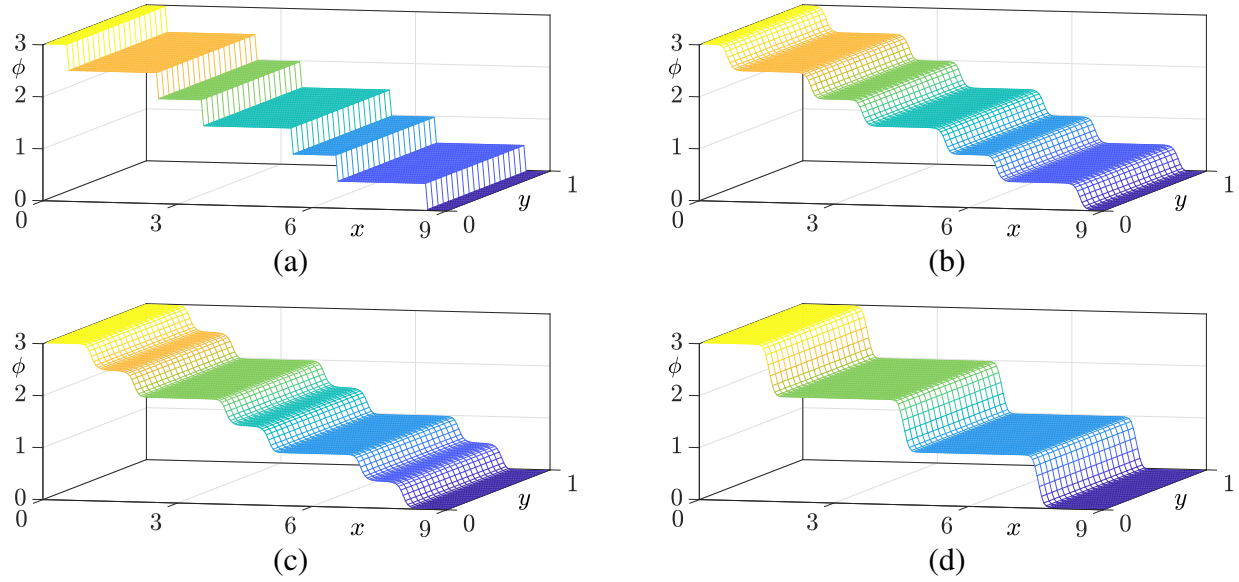

Figure 6. (a), (b), (c), and (d) are traveling wave solutions at $t = 0$, $10\Delta t$, $50\Delta t$, and $120\Delta t$, respectively, for $\alpha = 6$.

3.5. Nested rectangular phases with random perturbations

In this experiment, we define the initial condition $\phi(x, y, 0)$ on the domain $\Omega = (0, 6) \times (0, 3)$ as

$$\phi(x, y, 0) = \begin{cases} 0, & \text{if } 0.4 < x < 1.1 \text{ and } 0.4 < y < 1.1, \\ 1, & \text{if } 1.9 < x < 2.6 \text{ and } 1.9 < y < 2.6, \\ 2, & \text{if } 3.4 < x < 4.1 \text{ and } 0.4 < y < 1.1, \\ 3, & \text{if } 4.9 < x < 5.6 \text{ and } 1.9 < y < 2.6, \\ 0.5 + \text{rand}(x, y) & \text{if } x < 3 \text{ and outside the above regions}, \\ 2.5 + \text{rand}(x, y), & \text{if } x \geq 3 \text{ and outside the above regions}, \end{cases}$$

where rand(x, y) is a random number between -0.2 and 0.2. We use $N_x = 200$, $N_y = 100$, $h = 0.03$, $\Delta t = 0.0005$, and $\epsilon = 10h/\sqrt{\alpha}$. Figure 7 illustrates the temporal evolution of numerical solutions for $\alpha = 2$ and $\alpha = 6$. In Fig. 7, from top to bottom, the solutions are plotted at $t = 0$, $10\Delta t$, $100\Delta t$, and $400\Delta t$. The numerical results demonstrate that a larger α value improves the phase separation, which results in clearer and more distinct phase boundaries. This behavior is consistent with previous tests using a high-order double-well potential [13] and represents a valuable feature for data classification applications, as it exhibits robustness against noisy data.

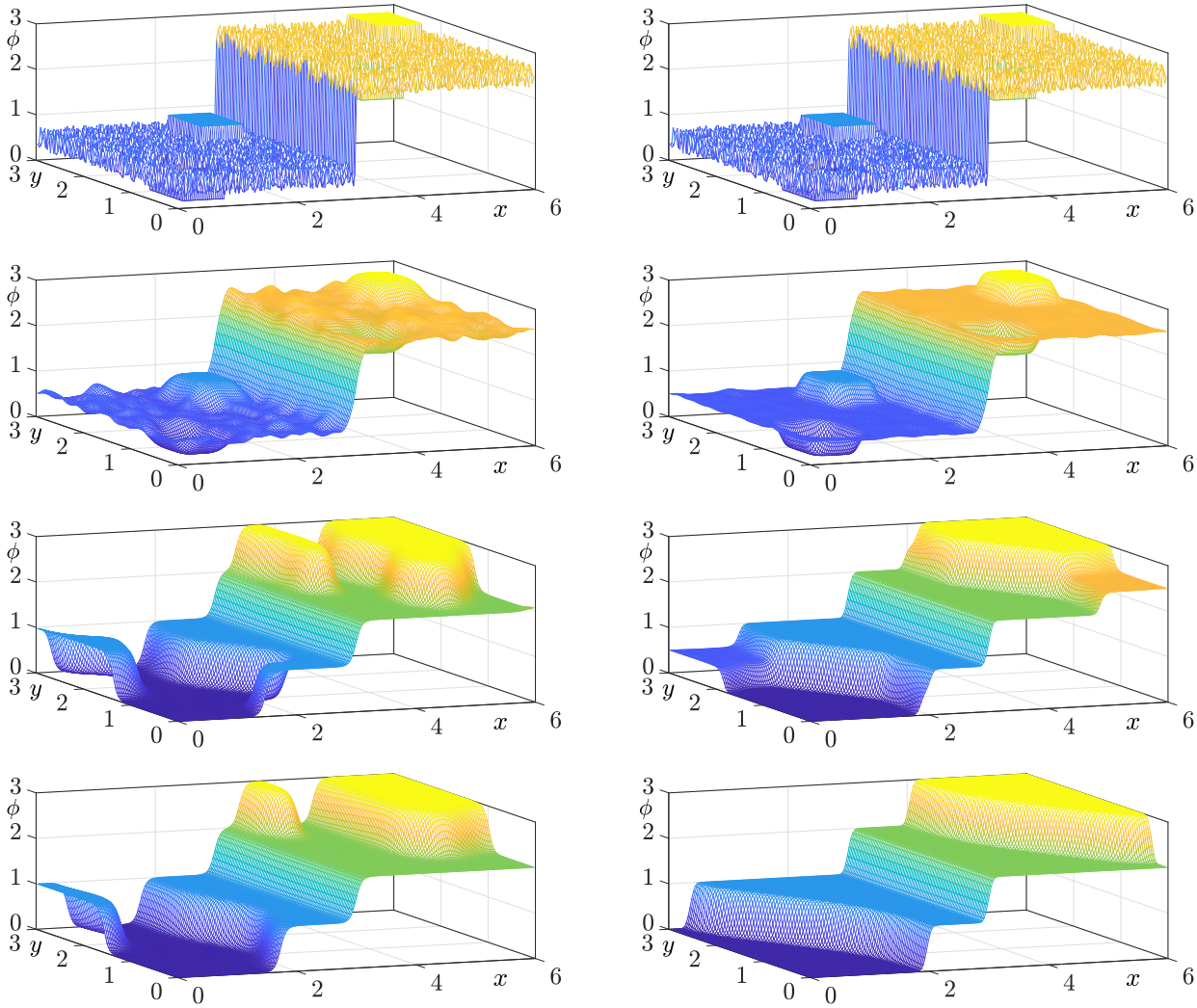

Figure 7. (a) and (b) are computational solutions for $\alpha = 2$ and $\alpha = 6$, respectively. From top to bottom, the solutions correspond to $t = 0$, $10\Delta t$, $100\Delta t$, and $400\Delta t$.

4. Conclusions

A numerical scheme is developed for the gradient flow of the MM functional using an operator-splitting method. The linear term is advanced with a Fourier spectral discretization, and the nonlinear term is updated via an analytically derived discrete formula based on Eq (2.4). The scheme is unconditionally stable and preserves pointwise boundedness for arbitrary time-step sizes. We systematically analyze the influence of the interface-width parameter ϵ on the flow. Numerical experiments, including mean curvature motion simulations, convergence studies showing spectral accuracy in space and first-order accuracy in time, and stability tests, confirm the robustness and accuracy of the proposed method.

Use of AI tools declaration

The authors declare they have not used Artificial Intelligence (AI) tools in the creation of this article.

Acknowledgment

The first author (Hyundong Kim) was supported by Basic Science Research Program through the National Research Foundation of Korea(NRF) funded by the Ministry of Education (RS-2025-25415913, NRF-2021R1A6A1A03044326). Junseok Kim was supported by the National Research Foundation(NRF), Korea, under project BK21 FOUR. The authors would like to thank the reviewers and academic editor for their valuable comments and constructive suggestions, which have greatly improved the quality of this paper.

Conflict of interest

The authors declare there is no conflict of interest.

Data Availability

The data used to support the findings of this study are available from the corresponding author upon request.

References

1. L. Modica, S. Mortola, Un esempio di Gamma-convergenza, *Boll. Unione Mat. Ital. B*, **14** (1977), 285–299.
2. H. Wilbuer, P. Kurzeja, J. Mosler, Phase field modeling of hyperelastic material interfaces–Theory, implementation and application to phase transformations, *Comput. Methods Appl. Mech. Eng.*, **426** (2024), 116972. https://doi.org/10.1016/j.cma.2024.116972
3. A. Aspri, A phase-field approach for detecting cavities via a Kohn–Vogelius type functional, *Inverse Probl.*, **38** (2022), 094001. https://doi.org/10.1088/1361-6420/ac82e4
4. J. Wang, J. Kim, A novel modified Modica–Mortola equation with a phase-dependent interfacial function, *Int. J. Mod. Phys. B*, **36** (2022), 2250055. https://doi.org/10.1142/S0217979222500552
5. Y. Li, S. Yoon, J. Wang, J. Park, S. Kim, C. Lee, et al., Fast and efficient numerical finite difference method for multiphase image segmentation, *Math. Probl. Eng.*, (2021), 2414209. https://doi.org/10.1155/2021/2414209
6. Y. Giga, J. Okamoto, M. Uesaka, A finer singular limit of a single-well Modica–Mortola functional and its applications to the Kobayashi–Warren–Carter energy, *Adv. Calc. Var.*, **16** (2023), 163–182. https://doi.org/10.1515/acv-2020-0113
7. Y. Jin, S. Kwak, S. Ham, J. Kim, A fast and efficient numerical algorithm for image segmentation and denoising, *AIMS Math.*, **9** (2024), 5015–5027. https://doi.org/10.3934/math.2024243

8. Y. M. Jung, S. H. Kang, J. Shen, Multiphase image segmentation via Modica–Mortola phase transition, *SIAM J. Appl. Math.*, **67** (2007), 1213–1232. https://doi.org/10.1137/060662708

9. B. Bogosel, D. Bucur, I. Fragalà, Phase field approach to optimal packing problems and related Cheeger clusters, *Appl. Math. Optim.*, **81** (2020), 63–87. https://doi.org/10.1007/s00245-018-9476-y

10. S. Ham, S. Kwak, C. Lee, G. Lee, J. Kim, A second-order time-accurate unconditionally stable method for a gradient flow for the Modica–Mortola functional, *J. Sci. Comput.*, **95** (2023), 63. https://doi.org/10.1007/s10915-023-02198-2

11. Z. Cao, Z. Weng, S. Zhai, An effective operator splitting scheme for general motion by mean curvature using a modified Allen–Cahn equation, *Appl. Math. Lett.*, **163** (2025), 109472. https://doi.org/10.1016/j.aml.2025.109472

12. G. Peng, Y. Li, An energy stable bound-preserving finite volume scheme for the Allen-Cahn equation based on operator splitting method, *Comput. Math. Appl.*, **178** (2025), 47–60. https://doi.org/10.1016/j.camwa.2024.11.014

13. J. Kim, Modified Wave-Front Propagation and Dynamics Coming from Higher-Order Double-Well Potentials in the Allen–Cahn Equations, *Mathematics*, **12** (2024), 3796. https://doi.org/10.3390/math12233796

14. Y. Hwang, I. Kim, S. Kwak, S. Ham, S. Kim, J. Kim, Unconditionally stable monte carlo simulation for solving the multi-dimensional Allen–Cahn equation, *Electron. Res. Arch.*, **31** (2023), 5104–5123. https://doi.org/10.3934/era.2023261

15. Y. Hwang, S. Ham, C. Lee, G. Lee, S. Kang, J. Kim, A simple and efficient numerical method for the Allen–Cahn equation on effective symmetric triangular meshes, *Electron. Res. Arch.*, **31** (2023), 4557–4578. https://doi.org/10.3934/era.2023233

16. H. G. Lee, A semi-analytical Fourier spectral method for the Swift–Hohenberg equation, *Comput. Math. Appl.*, **74** (2017), 1885–1896. https://doi.org/10.1016/j.camwa.2017.06.053

17. J. Choi, S. Ham, S. Kwak, Y. Hwang, J. Kim, Stability analysis of an explicit numerical scheme for the Allen–Cahn equation with high-order polynomial potentials, *AIMS Math.*, **9** (2024), 19332–19344. https://doi.org/10.3934/math.2024941

18. C. Zhang, H. Wang, J. Huang, C. Wang, X. Yue, A second order operator splitting numerical scheme for the "good" Boussinesq equation, *Appl. Numer. Math.*, **119** (2017), 179–193. https://doi.org/10.1016/j.apnum.2017.04.006

19. D. Li, C. Quan, J. Xu, Stability and convergence of Strang splitting. Part I: scalar Allen–Cahn equation, *J. Comput. Phys.*, **458** (2022), 111087. https://doi.org/10.1016/j.jcp.2022.111087